ACCEPTED VERSION

Emad Roshandel, Amin Mahmoudi, Wen L. Soong and Solmaz Kahourzade
Optimal Design of Induction Motors Over Driving Cycles for Electric Vehicles

Published version at:

http://hdl.handle.net/2440/140230

Optimal Design of Induction Motors Over Driving Cycles for Electric Vehicles

Emad Roshandel , *Member, IEEE*, Amin Mahmoudi , *Senior Member, IEEE*,
Wen L. Soong , *Senior Member, IEEE*, and Solmaz Kahourzade , *Member, IEEE*

Abstract—Consideration of the overload (OL) performance of electric machines designed for EVs enables increasing the power density of the propulsion system. This paper aims to show the characteristics and advantages of the optimal IMs which have the capability of handling OL. A subdomain model (SDM) with the capability of the saturation prediction is developed and validated using experimental data. A lumped thermal model is developed to predict the transient temperature variation of the IMs. The thermal model is validated using the Motor-CAD transient thermal analysis. The fast speed and accuracy of the applied SDM allows to select twelve variables in a large search space for the optimization purpose. Initially, an optimization procedure is proposed to design three IMs over three different driving cycles. The optimal designs are validated from the electromagnetic and thermal aspects by the finite element analysis. IMs are then designed optimally with consideration of the OL capability. A transient thermal analysis is carried out to validate the designs. The optimal designs with and without consideration of OL are compared in terms of the machine parameters and geometry to understand how dimensions and equivalent circuit parameters of the IMs vary according to the driving cycles. The comparison allows more intuition about the consideration of OL capability in design.

Index Terms—Driving cycle, electric vehicle, induction motor, lumped thermal model, machine design, optimization, subdomain model, thermal analysis.

LIST OF ABBREVIATIONS AND SYMBOLS

AFIM	Axial flux induction machine.
CIPS	California Instrument CSW series AC power source
CT	Constant torque
EffM	Efficiency map
EV	Electric vehicle
FEA	Finite element analysis
FEM	Finite element model
FW	Field weakening
HEV	Hybrid electric vehicle
HFET	Highway fuel economy test
IEC	International Electrotechnical Commission
IM	Induction motor
MEC	Magnetic equivalent circuit
MSE	Mean square error
NEMA	National Electrical Manufacturers Association
NYCC	New York City cycle
OL	Overload
PM	Permanent magnet
PMSM	Permanent magnet synchronous machine
PSO	Particle swarm optimization
RMSE	Root mean square error
SDM	Subdomain model
UDDC	Urban dynamometer driving cycle
VFD	Voltage frequency drive

List of Symbols

δ	Skin depth
$\theta_{W,\max}$	Maximum winding hotspot temperature
ρ	Conductor resistivity
μ_0	Air permeability
μ_r	Relative permeability of a material
A	Area of material normal to the heat flow direction
$CF1$	First cost function
$CF2$	Second cost function
C_p	Specific heat of the mass of material
D_i	Inner diameter
D_O	Outer diameter
D_{sh}	Shaft diameter
gOC	Global optimal cost
gr	Gear ratio
H_{er}	Height of the rotor end ring
it	Iteration number
$it_{\max}$	Maximum number of iterations
J	Current density
$J_{\max}$	Maximum current density
J_{rated}	Rated current density
k_{cd}	Thermal conductivity of each material
k_{con}	Convection factor
l	Axial length of the area of each part in thermal model
L_{ls}	Stator leakage inductance
L'_{lr}	Rotor leakage inductance referred to the stator side
L_{st}	Stack length
m	Material mass

N_{bar}	Number of rotor bars
N_{CT}	Number of operating points in the CT region outside the torque-speed envelope
N_{dr}	Total number of operating points within a driving cycle
N_{FW}	Number of operating points in the FW region outside the torque-speed envelope
N_{Ts}	Number of turns per slot
Nu	Nusselt number
Npop	Population size
OF	Objective function
$pbest$	Best particle position in an iteration.
P_{CT}	Penalty volume in the CT region
P_{FW}	Penalty volume in the FW region
Pr	Prandt Number
Q	Heat flow
r	Radius of each part in thermal model
r_{airgap}	Airgap radius
r_{BF-H}	Front bearing to case radius
r_{BR-F}	Rear bearing to flange radius
r_{R-b}	Rotor to bearing radius
r_{st-H}	Stator to housing radius
r_{w-st}	Winding to stator radius
r_w	Wheel radius
R_{BI}	Rotor back-iron
R_c	Core resistance
Re	Reynolds number
R_s	Winding resistance @ 60°C
R_r'	Rotor resistance referred to stator side @ 60°C
RS_h	Rotor bar height
RS_p	Rotor slot pitch
S	Effective area of each motor component
S_η	Average efficiency over driving cycle
S_{BI}	Stator back-iron
SS_h	Stator slot height
SS_p	Stator slot pitch
T	Temperature
T_A	Temperature at layer A
T_A	Temperature at layer B
Th	Material thickness between layers A and B
t	Time
ν	Vehicle linear speed
Vol_m	Volume of the IM
W_{er}	Width of the rotor end ring
X_{ls}	Stator leakage reactance referred to stator side @ 50 Hz
X_{mn}	Magnetizing reactance @ 50 Hz
X_{rp}	Rotor leakage reactance referred to stator side @ 50 Hz

II. INTRODUCTION

INDUCTION motors could be a suitable choice for utilization in the propulsion systems of electric vehicles EV and HEVs. The absence of rare-earth PM materials in the IMs leads to reduction of the machine cost in comparison to the PMSMs [1]. The literature shows that the performance parameters and efficiency of IMs during operation in the constant power region is comparable or even better than PMSMs [2].

The design of the IMs for the industrial line-starting or single point operation applications is a well-established subject. Unlike operation over a wide speed range, NEMA and IEC have standardized the design of IMs for line-start applications [3], [4]. The optimum geometry and dimensions to achieve the required performance in line-starting applications has been described in the literature.

The literature has introduced sizing equations of IMs for various geometries and power ratings [5]. These empirical formulae are prone to errors due to poor estimation of IM equivalent circuit parameters. On the other hand, these equations are developed based on the machine performance during operation at a single operating point (i.e., certain saturation level). So, the obtained model based on these equations is not valid for a wide range of operating points when saturation phenomenon in iron parts is involved. Consequently, the previous optimization studies, which have utilized sizing equations, were not able to provide an optimal IM for operation over a wide range of loads.

FEM-based motor optimization techniques have been the subject of extensive research. For PM machine optimization, FEA and electric equivalent circuits were used for optimal design of PM machines using a differential evolution algorithm [6]. The authors optimize a coreless linear PM machine using FEA and a genetic algorithm in a multi-objective optimization study [7]. Multi-objective optimization problems were simplified using the aggregation tree method, as suggested in [8]. The dependency of these articles on FEA is the main drawback because of their computational burden.

Surrogate models like the Gaussian Process (Kriging), which are a type of supervised machine learning, has been used as an effective tool in the design of electric machines [9], [10], [11]. These models have been used for reduction of the time of optimization study while using FEA [12]. These models require the previously collected data to predict the behavior of an electric machine. A number of FEA simulations are executed to gather the initial data from a case study [10]. Then, the collected data is used to predict the performance parameters in different geometries. The trained model by the surrogate model is used in a single- or multi-objective optimization problem to design the target machine based on the OF) and constraints [13], [14], [15]. In [16], a comprehensive study on the robust optimization of the electric machine were conducted. The authors showed that the robust optimization allows finding the optimum design which meets all the constraints with greater computational cost compared to the conventional optimization methods. The preparation of the required sample data for the surrogate models is computationally expensive because it needs the execution of a larger number of simulations. To reduce the number of simulations, previous studies have limited the number of the variables and their range of variation. The limited range of search however produces a design which may not be the global optima in the entire search space.

The use of analytical models like MEC [17], [18] and SDMs [19], [20] can be considered as a substitute for FEA to decrease the computational time of the optimization study. A MEC model

will become more accurate if the number of considered perme-ances are increased in the airgap and iron parts [21]. The increase of the number of elements leads to the increase of computational time. Most of the previously introduced MECs and SDMs ignore the saturation effect during the machine modelling [22], [23], [24]. The ignorance of the saturation reduces their accuracy for predicting the performance parameters over a driving cycle, particularly in the overload condition.

There are several references which introduced an approach for saturation modelling in SDMs [25], [26], [27], [28], [29], [30]. Only in [27], [30], the saturation model of the axial flux IM (AFIM) was employed in the optimization problems. The optimal design of line-start AFIMs have been discussed in [27] which means the results are not optimal for operation over driving cycles. In [30], the authors have considered a limited region near the nominal points for saturation modelling. Hence, the predicted performance cannot be reliable for all operating points in a driving cycle. The maximum torque per ampere control has been employed for the optimization in [30]. The maximum torque per ampere control cannot find the maximum efficiency points in the constant power region [31]. So, the designed AFIMs in [30] are not the optimal designs from the maximum efficiency perspective.

The effect of rotor losses on the machine temperature is another important factor which has been ignored in [27], [30]. Rotor losses in induction machines are often high which leads to a higher rotor temperature rise. The optimization studies in [30] assume a cooling system similar to the radial flux machines for their designs. Even if the assumed cooling system works successfully for the stator of the axial flux IMs, it cannot be used for the cooling of the rotor. This is because the available contact surface between the cooling channel and rotor in AFIM is less than the radial rotors, but also as the heat distribution on the disk (AFIM rotor) is different to a cylinder (radial flux IM rotor).

The contributions of this paper can be divided into the fol-lowing major and minor categories:

- Major Contributions:
  - √ Development and experimental validation of SDM con-sidering iron saturation suitable for design of IMs over a driving cycle.
  - √ Development of a lumped thermal model using the thermal modules in MATLAB/SIMULINK integrated with the proposed SDM model to predict the transient temperature variation of IMs.
- Minor Contributions:
  - √ A comparative study of the IM designs with and without consideration of the OL capability.
  - √ A detailed discussion on the consideration of OL capa-bility for IM designs indicating the tradeoffs between size and performance.

The fast speed of the SDM allows choosing twelve different variables in the optimization study. A similar cooling system as the 150 kW e-mobility IM [32], [33] is assumed for the design process. In the optimization study, the maximum loss of the rotor and stator are set as constraints to guarantee the success of the cooling system at the rated condition. The loss

TABLE I
STUDIED IM ELECTRICAL CHARACTERISTICS AND GEOMETRY

Electrical Characteristics			
Rated line voltage [V]	415	Rated power [W]	2200
Frequency [Hz]	50	Number of poles	4
Geometry and dimensions			
Stator outer diameter [mm]	165	Stator inner diameter [mm]	105
Rotor outer diameter [mm]	104	Rotor inner diameter [mm]	38
Number of stator slots	36	Number of rotor slots	28
Stator slot height [mm]	12.8	Width of stator slot opening [mm]	2.8
Airgap length [mm]	0.47	Rotor slot height [mm]	18.21

constraint is determined based on the maximum loss per outer stack of the stator and rotor of the benchmark design (i.e., 150 kW e-mobility IM). A single-speed transmission system with a gear ratio of 9.6 is assumed between the motor shaft and wheels. An optimization problem to obtain the maximum efficiency over the driving cycle in the minimum volume is defined. The optimal designs are validated against the FEA results in terms of their electromagnetic and thermal performance. In the second stage, the proposed optimization procedure is utilized to design IMs with consideration of the OL capability over the driving cycle. The developed lumped model is used to predict the hotspot temperature of the winding in the optimization study to check the temperature limit. The obtained results clarify how the OL capability consideration can reduce the IM volume while the thermal constraints over the studied driving cycle are met.

The experimental validation of the SDM model is carried out in Section III. The proposed lumped thermal model is dis-cussed and validated in Section IV. The considered optimization problems and their procedures is described in Section V. The introduced optimization problems are executed on three different driving cycles in Section VI. The discussion on the difference of the optimal designs with and without investigation of OL are provided in Section VI.

III. SDM MODEL PREPARATION AND VALIDATION

A subdomain model which calculates the Maxwell equations in five subdomains in IMs was introduced in [23]. The perfor-mance parameter prediction capability was improved by adding modeling of the saturation level in the iron parts at different loadings. In [25], the model accuracy was validated using 2-D and 3-D FEA results. In this section, this model is developed and validated using experimental results.

A 2.2 kW, 4 pole, 415 V induction machine is considered for the validation of the SDM. The dimensions and characteristics of this machine are tabulated in Table I. This is a commercial machine and information was not available about the B-H curve and loss curve of the lamination material and so M250 steel is assumed. Fig. 1 shows the prepared experimental setup in-cluding a dynamometer motor, test motor, dynamometer, and high precision power analyzer. The dynamometer motor acts as a load for the motor and is controlled with a voltage frequency drive (VFD). The dynamometer provides the torque and speed feedback for the VFD as well as the measurement data for the power analyzer.
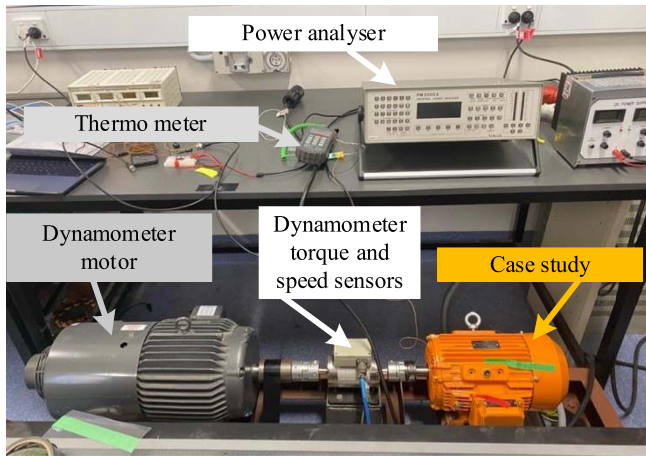
Fig. 1. The experimental setup for verification of the proposed SDM model. A 2.2kW IM is used for validation.

TABLE II
EQUIVALENT CIRCUIT PARAMETERS FOR THE STUDIED 2.2kW MACHINE OBTAINED FROM NO-LOAD AND LOCKED ROTOR TESTS IN EXPERIMENT, FEA ANALYSIS, AND THE PROPOSED MODEL

EEC parameters	Experimental results	2-D FEA	Proposed model
R_s	2.52 Ω	2.52 Ω	2.71 Ω
R'_r	2.77 Ω	2.56 Ω	2.46 Ω
X_{ls}	3.29 Ω	3.37 Ω	3.39 Ω
X_{rp}	3.29 Ω	3.37 Ω	3.45 Ω
X_{mn}	123 Ω	127 Ω	127 Ω
R_c	2.05 kΩ	2.01 kΩ	1.96 kΩ

The test motor is supplied by an autotransformer. The input power of the test machine is measured using a Voltech power analyzer (PM3000ACE) [34]. This accepts the speed and torque inputs in addition to the electrical signals for measurement of the output mechanical power.

Table II presents the experimentally obtained equivalent circuit parameters from the no-load and locked rotor tests. The results of the analytical model are in a good agreement with the experimentally calculated equivalent circuit parameters. The experimental data has been collected when the stator and rotor winding temperatures were at about 60 °C. The SDM resistances are also calculated at 60 °C. In the 2-D FEA model, the measured resistance from the stator is chosen for the simulation. Also, the 60°C temperature is considered for calculation of the end-ring resistance according to [25].

The capability of the model to predict the saturation curve of the studied motor is validated by collecting the no-load test data at 1500 rpm with line voltages up to 500 V. Fig. 2 compares the experimental, proposed SDM, and FEA results in the no-load operating condition. The measured and calculated current at different voltage levels is presented in Fig. 2(a). Fig. 2(b) shows the error of the estimated current by the proposed model. In the worst-case voltage, the error of the proposed model is about 40%. The calculated MSE for current prediction using SDM and FEA models are respectively 0.0685 and 0.0293. It means the maximum RMSE for these models are 0.26 and
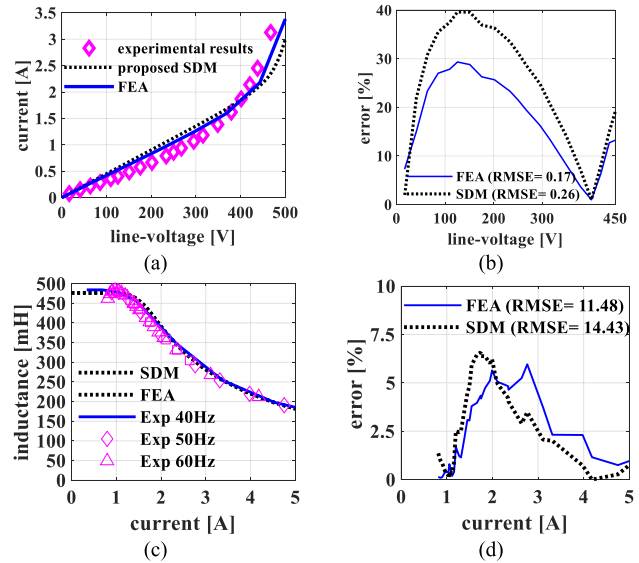

Fig. 2. No-load experimental results: (a) no-load current vs voltage, (b) no-load current error vs voltage using SDM versus FEA, (c) stator inductance variation at different frequencies vs. no-load current, (d) the inductance error vs. current using SDM versus FEA.

0.17, respectively. Such errors are considered acceptable for 2.15A rated magnetizing current. The difference between the B-H curve characteristics of the assumed steel and the utilized steel and the difference between the real and simulated airgap lengths contributes to these errors.

The motor is next driven by a California Instrument CSW series AC power source (CIPS) which produces variable frequency sinusoidal waveforms. The machine is supplied with 40 Hz, 50 Hz, and 60 Hz by the CIPS in the no-load condition. The obtained stator inductance in the no-load test at these frequencies as a function of current is plotted in Fig. 2(c). This figure demonstrates the proposed model capability of predicting the machine inductance. Note that due to the large slip at the lower supply voltage levels, the experimentally collected inductance shows small errors at low currents. Fig. 2(d) shows the maximum error of the estimated inductance which are about 6% and 16% for the proposed SDM and FEA models. The maximum error of the FEA occurs at high saturation levels where the machine does not normally operate. The proposed SDM and FEA RMSE values are 14.4 and 17.5, respectively. These values are acceptable for the inductance range of 165 mH to 483 mH.

The collected experimental data as a function of load torque is compared with proposed model in Fig. 3. The supply current, shaft speed, output power, and efficiency of the machine shown have an acceptable agreement with the calculated values. The maximum error of the current does not exceed 6% (around the rated load of 14.5 Nm). The error of the estimated speed and power are less than 1%, except in the low power region. The maximum error of the 5.5% happens at 14.8Nm point in the efficiency curve. This efficiency error likely resulted from the larger current flowing through the winding and rotor cage.
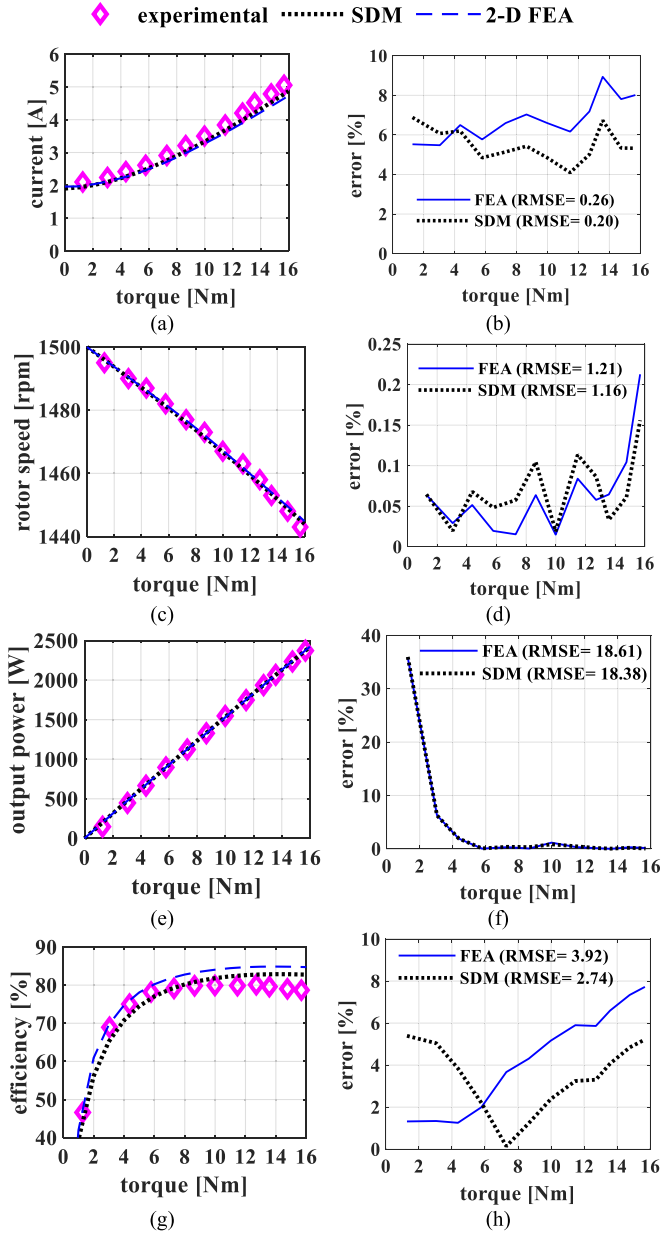
Fig. 3. Loaded performance validation: (a) and (b) current and current error variations vs. load; (c) and (d) speed and speed error variations vs. load; (e) and (f) output power and output power error variations vs. load; (g) and (h) efficiency and efficiency variations error vs. load.
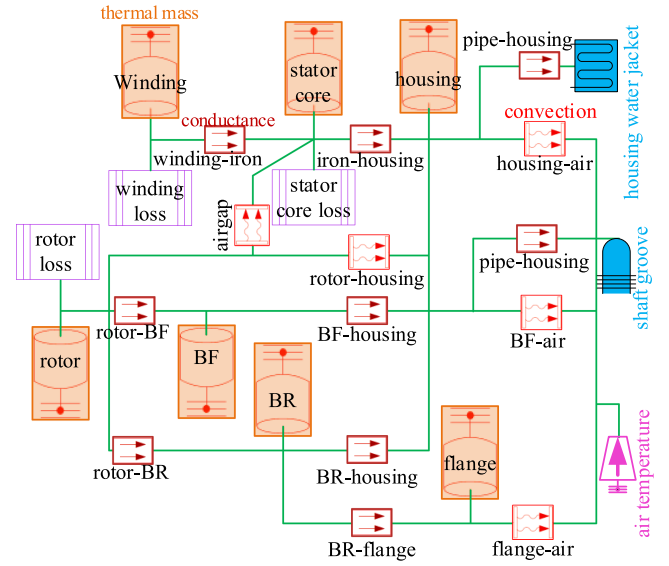

Fig. 4. The developed lumped thermal model for the transient thermal analysis of the induction machine.

TABLE III
THE THERMAL PARAMETERS USED FOR THE THERMAL ANALYSIS

Specific heat for each part (C_p)			
Winding [J/kg/K]	385	Housing [J/kg/K]	733
Stator iron [J/kg/K]	460	Bearing [J/kg/K]	447
Rotor iron [J/kg/K]	460	Flange [J/kg/K]	447
Thermal conductivity of each part (k_{cd})			
Winding – Iron [W/(m×K)]	401	Bearing – Housing [W/(m×K)]	80.2
Iron – Housing [W/(m×K)]	80.2	Bearing – Flange [W/(m×K)]	25.5
Rotor – Bearing [W/(m×K)]	25.5		
Convection heat transfer coefficient (k_{con})			
Airgap [W/(m²×K)]	250	Bearing – Air [W/(m²×K)]	125
Housing – Air [W/(m²×K)]	26.8	Flange – Air [W/(m²×K)]	125
Reynolds (*Re*) and Prandtl (*Pr*) numbers for cooling channels			
Re	16E5	*Pr*	11.7

IV. THERMAL MODEL AND VALIDATION

A. Thermal Model for Temperature Prediction

A lumped parameter model, shown Fig. 4, is developed to predict the thermal behavior of the induction machine over the driving cycle. The generated heat because of the stator winding loss, stator core loss, and rotor cage and iron losses are represented by the heat flow sources in the model. The convection heat transfer, thermal conductance, and thermal masses are utilized to develop the thermal model.

The thermal mass which is the material's capability in absorbing and releasing the thermal heat is used for different parts of the machine including winding, stator iron, motor housing, rotor iron, bearings, and flange. A conduction path is considered between those parts which are physically connected with each other. Convection heat transfer is used where the heat is transferred through the air.

The heat flow due to the thermal mass as a function of time (t) is defined by (1) where Q is the heat flow, C_p is the specific heat of the mass of material, m is the material mass, and T is the temperature. The considered specific heat and the density of each material are reported in Table III.

$$Q(t) = mC_p \frac{dT}{dt} \qquad (1)$$

The Fourier law presented in (2) is utilized to describe the conductive heat transfer. The thermal conductivity of each material (k_{cd}) used in this paper is tabulated in Table III. In (2), A is the area of material normal to the heat flow direction. This area for each section is found using (3) where r is the considered radius for calculation of the area and l is the axial length of each part. The winding to stator radius, stator to housing radius, rotor to
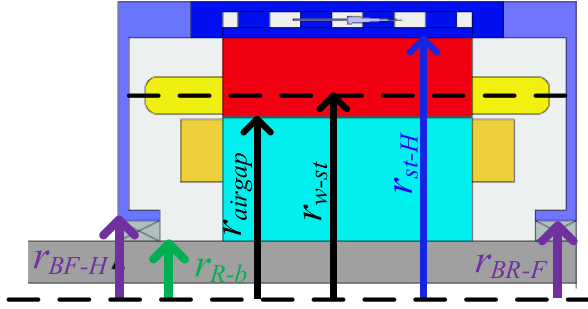
Fig. 5. The considered radii for calculation of the area for each part of the machine.

bearing radius, front bearing to case radius, and rear bearing to flange radius are shown by $r_{w-st}, r_{st-H}, r_{R-b}, r_{BF-H}, r_{BR-F}$, respectively in Fig. 5. The material thickness between layers A and B and the temperatures at layers A and B are shown by Th, T_A, and T_B.

$$Q(t) = k_{cd} \frac{A}{Th} (T_A(t) - T_B(t)) \tag{2}$$

$$A = 2\pi r l \tag{3}$$

The convection heat transfer is modelled by Newton's law of cooling formulated in (4). In (4), k_{con} is the convection heat transfer coefficient. Note that the S is the effective area of each motor component. For instance, the rotor area is $S = 2\pi(r_{airgap}^2 - r_{R-b}^2)$; two times the effective rotor surface is considered because the rotor convection to the housing occurs at both ends of the rotor. The reported k_{con} for air is the considered coefficient for the flange, bearing, and housing convection. According to Taylor and Gazler [35], for Taylor numbers less than 41, the heat transfer is only conductive in the airgap and the Nusselt number (Nu) is equal to 2 [35], [36]. Considering this, k_{con} in the airgap is found by multiplication of the air convection coefficient and 2 (i.e., the Nusselt number).

$$Q(t) = k_{con} S (T_A(t) - T_B(t)) \tag{4}$$

It is assumed that the ethylene glycol-water mixture flows through the spiral cooling channel and shaft groove with a constant flow rate. The pipe (TL) block from the MATLAB SIMULINK library is used to model the heat transfer at the pipe wall. This block uses the Dittus-Boelter correlation which estimates the Nu as a function of the Reynolds (Re) and Prandt (Pr) numbers. The laminar flow and rectangular channel equations presented in [37] are used to find the Nusselt number for the rotor groove cooling and stator spiral cooling. The values of the Re and Pr in calculating Nu are given in Table III.

B. Introduction of Benchmark IM

An IM with a rating of 100 kW continuous power (at current density of 16 A/mm^2 and DC-link voltage of 400 V) and 150 kW peak power (at 50 A/mm^2 current density) is considered as the benchmark machine in this study [32], [33]. This commercial machine has 72 stator slots and 84 copper rotor bars. The

lamination material M250-35A is used in the construction of stator and rotor.

The stator of this machine is cooled by a 50/50 water/glycol mixture which flows through a spiral cooling jacket. The coolant inlet temperature is 65°C and a 6.5 l/min flow rate is used. A spiral groove is assumed into the shaft which carries coolant at 2 l/min.

The stator loss of the benchmark design at rated power is 1.8 kW. The available outer surface of the machine cooled by the spiral cooling is 0.094 m^2. Thus, the maximum permitted loss per outer stack for this machine 15.2 kW/m^2 which will be used as a limiting factor in the optimization study. It is assumed that the diameter of the rotor spiral groove of the designed machines in this paper is equal to the benchmark groove diameter (15 mm). So, the active length of the rotor which is in contact with the cooling system plays an important role to successfully remove the heat from the rotor. As the axial stack length (L_{st}) of the benchmark design is 0.12 m, 3.3 kW/m is considered as the allowable loss per length for the rotor.

The benchmark machine was designed for operation in a vehicle with a 1960 kg weight. The motor transfers power to the wheels through a single-speed gearbox with a 9.6 gear ratio (gr). The wheel radius for the drivetrain is $r_w = 0.35$m. Thus, for the linear speed of ν meter per second, the motor angular speed is obtained by (5) in rpm. This equation is considered to convert the given linear speed of the driving cycle to the motor operating speed in this paper.

$$\omega_m = \frac{\nu}{r_w} \times gr \times \frac{60}{2\pi} \tag{5}$$

C. Validation of the Thermal Model

The thermal model is validated through a transient thermal analysis. It is assumed that the benchmark machine is operated over the UDDC [38]. The performance parameters of the machine are calculated using the Motor-CAD software.

The Motor-CAD transient thermal analysis module is utilized to predict the machine temperature variation over the UDDC operating points. The obtained losses over the driving cycle are considered as the input for the introduced thermal model. The predicted results shown in Fig. 6 shows an acceptable agreement between Motor-CAD and the developed model results.

V. PROBLEM DEFINITION

A sequential process is introduced for optimal design of IMs with and without consideration of OL in a multi-physics environment. The proposed procedure benefits from the fast calculation speed and accuracy of both the SDM and thermal model. The results of the optimization study provide a good understanding of the differences in the optimal IM design with respect to different types of driving cycles.

Electric machine design problems are complex because of their inherent non-linear nature. As such, a large solution space should be defined to find the optimum results. Metaheuristic algorithms can efficiently search a wide solution space and identify near-optimal solutions that traditional optimisation methods cannot. The stochastic nature of PSO helps to converge to
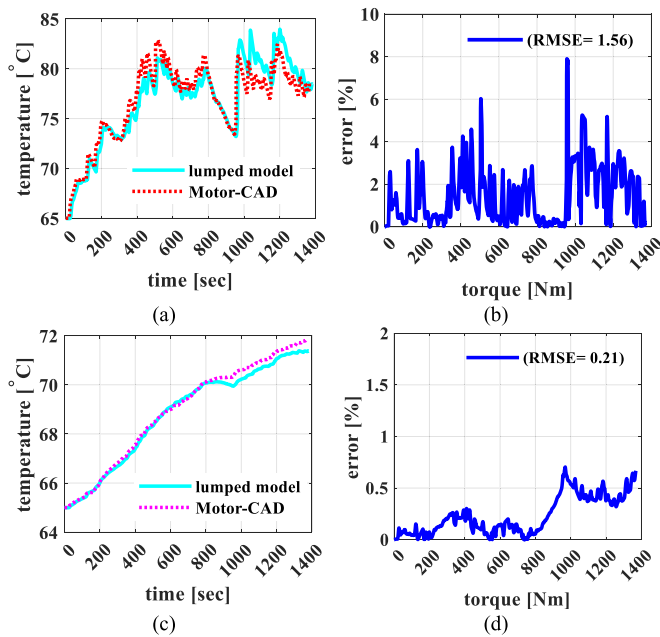
Fig. 6. Transient thermal analysis results for the developed lumped-circuit model versus the Motor-CAD predictions for the benchmark IM over the UDDC: (a) Stator hotspot temperature, (b) corresponding error, (c) rotor temperature, (d) corresponding error.

the global optima by selection of a sufficiently large solution population in the search space. The literature shows successful performance of the PSO in optimal design of electrical machines [39], [40], [41]. Hence, PSO is the proposed metaheuristic optimization algorithm in this study.

A. PSO Algorithm

PSO is a population-based optimization which iteratively updates a population of potential solutions (called particles) based on their best solution and the swarm's global best solution [42]. In each iteration, a velocity vector is calculated using the previous velocity and position of $pbest$ and $gbest$, and then used to direct the particles as they move through the search space. The global best solution is found after a stopping criterion such as a minimum error or maximum number of iterations.

Due to the stochastic nature of PSO, it may converge to local optimal solutions instead of finding the global optima. The literature shows PSO has a good convergence rate when the number of particles is equal to about thirty times of the number of parameters (variables) [43]. This study considers 12 variables in the optimization problem definition. So, a population size of 360 is selected for this problem.

The inertia weight is commonly a value between 0.4 to 0.9. In this problem, 0.9 is selected because the exploration rate is higher at larger values of inertia weight. The selected population size and damping factor allows better exploration of the search space. So, a small damping factor of 0.3 is used to enhance exploitation in the considered search space. The individual and social co-speeds of particles can be a number in the range of 1 to 2.5 [44]. An equal value of 1.6 is selected for the individual

TABLE IV
THE SELECTED PSO PARAMETERS IN THIS STUDY

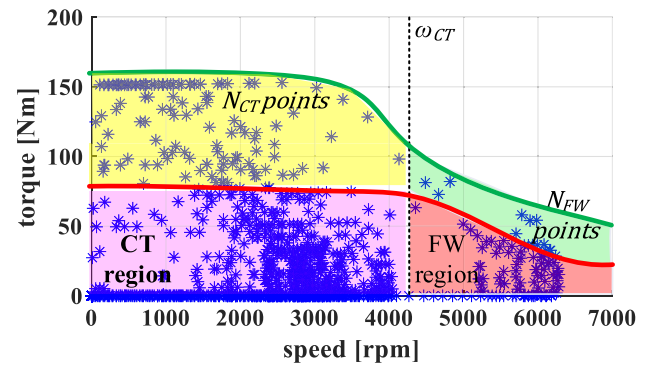| Parameter	Value	Parameter	Value
Number of variables	12	Population size	360
Number of iterations	50	Inertia weight	0.9
Damping factor	0.3	Social co-speed	1.6
Individual co-speed	1.6		

Fig. 7. Torque speed curve of a sample machine showing the CT and FW regions as well as the N_{CT} and N_{FW} points in a driving cycle.

and social co-speeds to a have a slower convergence rate with more exploitation.

The problem is defined for a certain number of iterations (it_{max}) and a value of 50 is chosen to enable the algorithm to converge to the optimal solution after the slow exploration and exploitation explained in the above. Table IV lists the selected PSO parameters for optimization problems in this study.

B. Definition of Optimization Problem Without Consideration of Overload Condition

This section describes an optimization procedure to find an optimal design without consideration of transient performance. The designed machine should be able to operate continuously at each single operating point (all blue stars presented in Fig. 7).

The flowchart of the defined optimization problem including the detailed steps have been presented in Fig. 8. The fast speed of calculation of the SDM allows selecting large number of variables in a wide search space. Number of turns, number of rotor bars, rotor slot width, stator slot width, rotor slot height, stator slot height, stator back-iron, rotor back-iron, end ring width, end ring height, stack length, stator slot opening are twelve considered variables for the optimization.

As shown in Fig. 8, the initial variables are randomly generated, and the problem is solved to provide the initial solution for the first iteration. Then, the problem is solved for the considered Npop in each iteration. In each loop, the particles' speed and position are updated to find the updated design dimensions for each loop.

It should be highlighted that the number of turns and rotor slot number must have a integer value. To apply the integer constraints, the selected solution in each iteration for these two values are rounded up.
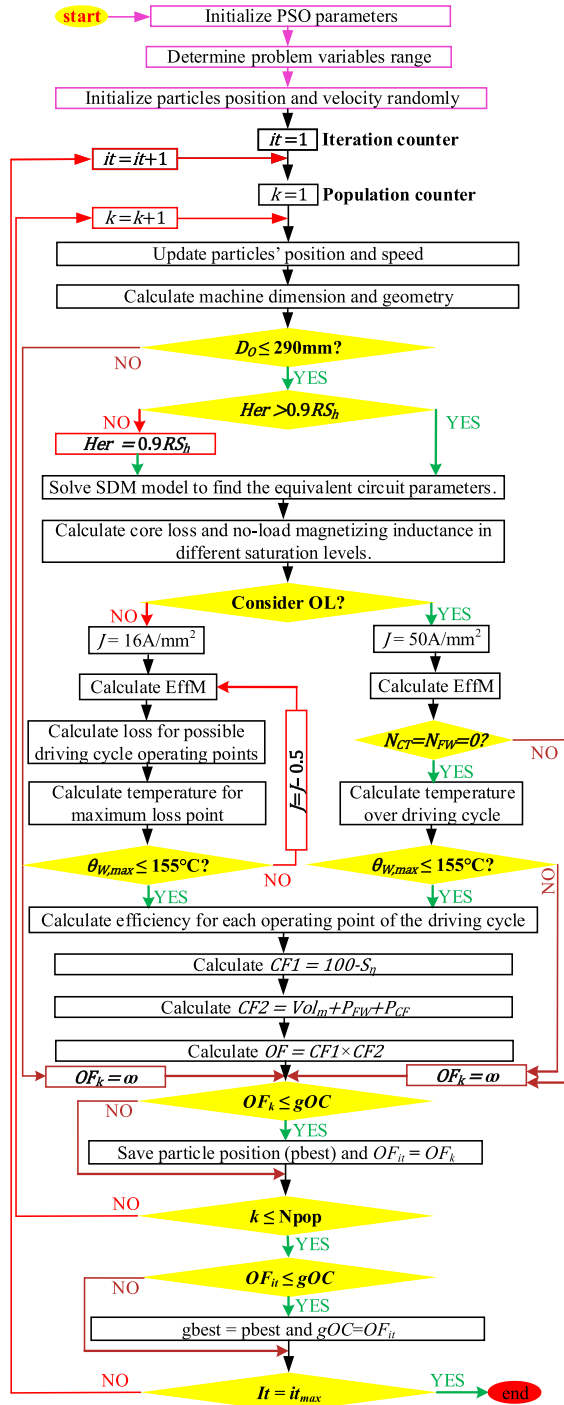
Fig. 8. The optimization study flowchart for consideration of the normal and overload conditions.

The developed SDM is used to find the magnetic vector potentials in each iteration. The core loss, saturation curve (i.e., voltage vs. current curve of the machine at no-load), and electric equivalent circuit parameters are found using the SDM. Based on the stator slot area in each iteration, the value of the maximum operating current of the machine is determined from the assumed 16 A/mm^2 current density.

The obtained current is set as the rated current for the machine. Considering this current and DC-link voltage of 400 V, the maximum efficiency control is applied to obtain the efficiency map (EffM).

The total loss of the machine for all operating points in a driving cycle is calculated. The maximum loss point is selected. The winding, cage, and core losses are obtained for the maximum loss point. They are the inputs to the thermal model. The thermal model is executed for entire time of the simulation. The obtained winding temperature is used for checking the hot spot temperature limit. If the winding temperature exceeds the loss limits, the rated stator winding current density is reduced. This process is repeated. Once the temperature limit is met, the algorithm directs the analysis into the next stage.

The calculated EffM is used to find the efficiency of each of the operating points in the considered driving cycle. The first cost function ($CF1$) aims to maximize the efficiency of the operating points. To find $CF1$, the average efficiency over driving cycle (S_η) is found and then is subtracted from 100%.

In Fig. 7, the red line shows the rated torque-speed curve of an IM. So, the machine rated torque-speed curve must cover all operating points to achieve an optimal design without consideration of transient performance.

This objective is achievable when the machine volume is increased. If the volume is not considered as the second objective function, the PSO will apply a large increase in volume to find the optimum design. This large increase may result in convergence to a local minimum in large machine volumes.

To reduce the risk of being trapped in a local minimum, the volume is penalized in both the CT and FW regions. The CT region includes the operating points below the rated speed of ω_{CT} (see Fig. 7), while the machine operating region beyond this speed is called FW. The number of operating points located above the CT and FW regions are separated and counted by N_{CT} and N_{FW}, respectively. The regions enclosing the N_{CT} and N_{FW} points are highlighted by yellow and green in Fig. 7. The volume of the IM which is evaluated in the current iteration is shown by Vol_m, which is the summation of the volumes of the rotor, stator and end winding. The considered penalty for the N_{CT} points is calculated by (6).

$$P_{CT} = N_{CT} \times Vol_m \qquad (6)$$

The compensation of the torque at the field weakening (FW) region by increasing the current is limited due to the voltage limit. Hence, the penalty volume (P_{FW}) for the N_{FW} points is applied by a larger volume factor. According to (7), two times of N_{FW} is applied to the volume penalty.

$$P_{FW} = 2N_{FW} \times Vol_m \qquad (7)$$

The maximum D_O of 290 mm is set as a constraint for the targeted machine. For this reason, this constraint is checked at the beginning of each iteration. If this constraint is not met, the algorithm rejects the design by setting its OF value to infinity.

As the height of the rotor end ring is a maximum of 0.9 times of the rotor bar height, this value is also checked in each iteration. If the selected value for H_{er} is larger than RS_h, the selected H_{er} value is limited to this value.

To make the second cost function the Vol_m is summed up with the obtained penalties applied to volume ($CF2 = Vol_m + P_{FW} + P_{CF}$). The objective function is defined by the multiplication of the $CF1$ and $CF2$ (i.e., $OF = CF1 \times CF2$). Finally, the optimum solution which gives the minimum objective function is chose as the best solution at the end of each iteration. The described optimization process is summarized and modeled as follows:

$$\text{Minimize}: OF = CF1 \times CF2$$

$$\text{Subject to} \begin{cases} D_O \leq 290\text{mm} \\ \theta_{W,\max} \leq 155\,°\text{C} \end{cases} \quad (8)$$

As Class F insulation is assumed for the stator winding, 155 °C is considered as the maximum permitted temperature for the winding hotspot.

C. Consideration of Overload Capability During Optimization

In a given driving cycle, there are many operating points where the machine torque is low that provides time for cooling. This allows increasing the loss limit of the machine in the transient operation over the driving cycle. According to Fig. 8, the process of the consideration of the OL capability follows a different step compared to the normal design based on maximum power.

In the OL consideration procedure, a similar current density as the benchmark IM (i.e., 50 A/mm^2) is assumed at the first step. The rotor loss, stator winding loss, and stator core loss maps and EffM of a machine in each iteration are calculated.

The transient loss estimation is feasible if all operating points of the driving cycle are covered by the EffM. Thus, if N_{CT} or N_{FW} are non-zero, the IM is rejected by setting its OF to infinity. This criterion, summarized in (9), is defined as a problem constraint.

$$\begin{cases} N_{CT} = N_{FW} = 0 \to \text{accept design} \\ N_{CT} \neq 0 \text{ or } N_{FW} \neq 0 \to \text{reject design (i.e., } OF = \infty) \end{cases} \quad (9)$$

The transient loss variation of each part of the machine over a driving cycle is extracted from the loss map. The proposed thermal model is used to predict the machine temperature variation using the transient loss data. If the maximum temperature of the design meets the Class F insolation temperature standard (i.e., $\theta_{W,\max} \leq 155°\text{C}$), then the design is accepted.

The algorithm continues its process to find $CF1$ and $CF2$ using the same procedure as the normal design described in the previous section. Thus, the optimization process with OL consideration is modelled as follows:

$$\text{Minimize}: OF = CF1 \times CF2$$

$$\text{Subject to} \begin{cases} D_O \leq 290 \text{ mm} \\ N_{CT} = N_{FW} = 0 \\ \theta_{W,\max} \leq 155°\text{C} \end{cases} \quad (10)$$

VI. Optimization Results and Discussion

Three driving cycles including HFET, UDDC, and NYCC are considered for the optimization study [45]. The maximum
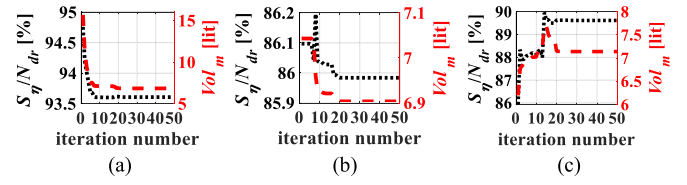

Fig. 9.   The variation of the efficiency over driving cycle and the active part of the at each iteration of the optimization. (a) HFET; (b) UDDC; (c) NYCC.

operating speed for the considered driving cycles is 7,000 rpm. Considering a 6-pole design based on the benchmark machine, the operating frequency of the designed machines is 350 Hz. Increasing the frequency reduces the effective copper area due to the skin effect which leads to a winding resistance increase [31]. To address this issue, a stranded winding which includes parallel paths is considered.

As formulated in (11), the skin depth depends on the resistivity and permeability of a conductor as well as the operating frequency.

$$\delta = \sqrt{\frac{2\rho}{2\pi f_{eff}\mu_r\mu_0}} \quad (11)$$

If 17.7 nΩ/m and 1 are considered for the copper resistivity and relative permeability, then for a frequency of 350 Hz, the skin depth is 3.6 mm. It is reasonable to select one third of the skin depth for the copper diameter to minimize the skin effect. To be consistent with the benchmark design 1.01 mm wire diameter is selected [32], [33] for the optimization study. This consideration allows to calculate the winding resistance using (11) in [25].

A. Normal Optimization

The normal optimization approach for the design of the IMs over the three driving cycles is executed to find the optimal IMs. The variables and their selected ranges in the solution space are reported in Table V.

The trend of the variation of the average efficiency over the driving cycle against volume during the optimization is presented in Fig. 9. According to this figure, the higher efficiency is achieved by increasing the volume. It is expected because with larger volumes the airgap area is larger which allows generating more torque with smaller currents. The reduction of the current decreases the ohmic losses which are a large portion of the losses in IMs. Thus, the efficiency will generally be increased by increasing the volume.

The gray rows in Table V shows the obtained dimensions of the optimal designs for each driving cycle. The stator inner and outer diameters (D_i and D_O) which are indirectly obtained from the optimization solutions are also reported in this table. It is seen that the optimization process tends to maximize the outer diameter which is expected as this allows reducing the ohmic losses due to the larger airgap area.

The designed machines are also simulated by the electric machine analysis Motor-CAD package to validate the accuracy of the SDM using FEA results. Fig. 10 shows the difference between the EffM of the designs calculated by the SDM with

TABLE V
THE OPTIMIZATION VARIABLE RANGES AND OPTIMAL SOLUTIONS

|		N_{Ts}	R_{bar}	RS_p	SS_p	L_{st} [mm]	D_{sh} [mm]	S_{BI} [mm]	R_{BI} [mm]	RS_h [mm]	SS_h [mm]	W_{er} [mm]	H_{er} [mm]	D_O [mm]	D_i [mm]	J_{rated} [A/mm²]	J_{max} [A/mm²]
Variable ranges		2-15	40-100	0.2-0.7	0.5-0.8	100-350	30-150	10-100	10-100	10-50	10-50	5-50	5-50	--	--	--	--
Optimal solutions	Norm HFET	3	66	0.39	0.58	152	63.6	21.4	22.0	23.9	20.9	10.1	12.3	243	157	11.4	--
	Norm UDDC	3	96	0.26	0.56	148	71.0	17.5	30.1	31.4	23.1	12.6	18.5	277	196	8.86	--
	Norm NYCC	3	78	0.47	0.55	230	98.9	16.7	31.2	21.1	25.7	15.3	19.8	287	201	8.96	--
	OL HFET	4	78	0.36	0.64	116	45.6	10.5	14.2	11.1	14.0	11.8	8.11	145	95.4	16.0	50.0
	OL UDDC	4	64	0.66	0.51	103	45.1	10.1	15.5	10.4	21.2	7.34	9.06	158	94.1	16.0	50.0
	OL NYCC	4	60	0.28	0.62	101	85.9	14.2	27.1	13.6	10.0	6.16	11.3	216	166	16.0	50.0
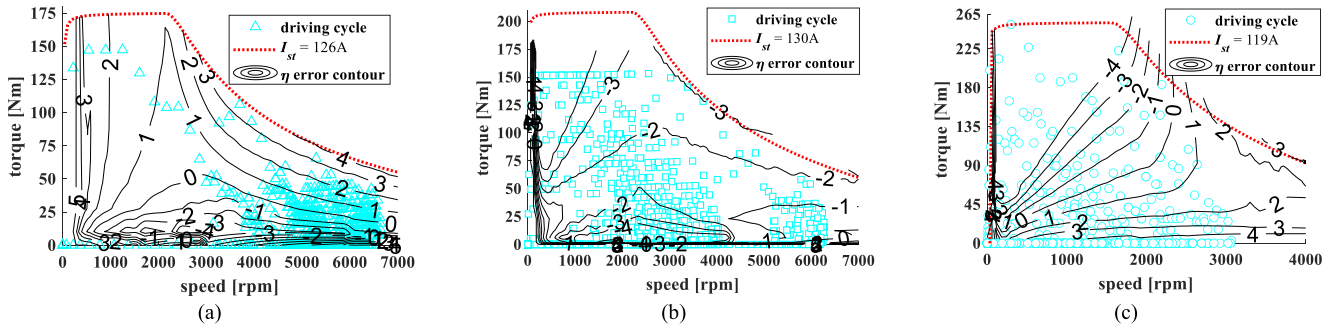
Fig. 10. (a), (b), and (c) the difference between the obtained EffMs from the analytical model and the Motor-CAD software results. The red dotted lines show the capability based on the rated current determined by the normal optimization study. The cyan points are the considered driving cycle points.
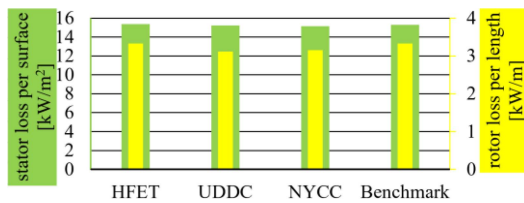

Fig. 11. The full load 2-D FEA results of the stator loss (in green) and rotor loss (in yellow) densities for the designed machines and benchmark.

the EffM obtained from FEA. It is observed that the largest difference between the predicted efficiency is less than 5%.

Fig. 11 shows that the thermal limits (i.e., total loss per outer stack area and rotor loss per rotor length) are considered during the optimization study and these values are approximately equal to the benchmark design.

The reliability of the design for operation with regards to temperature limits is another point which is studied in this section. A thermal analysis is executed on the designed machines in Motor-CAD. The results of the analysis shown in Fig. 12 demonstrate that the optimization produces the optimum design with acceptable temperature limits.

Fig. 12 shows the rotor of the designed IM for the HFET operates at a higher temperature at full load. This figure demonstrates that the rotor is the hottest part of all three designs. It shows the importance of the proper selection of the cooling system for the IM rotor.

The EffMs of the designs are calculated without considering mechanical losses and are presented in the third column of

Fig. 12. It is seen that the designed machines offer an efficiency larger than 90% in most of the driving cycle points in all designs. As increasing the current density leads to the increase of the ohmic losses, the optimization algorithm tries to keep the current density of these designs at moderate values (see Table V).

According to Fig. 12, the maximum torque of the designed machines is higher than the maximum torque of the driving cycle. However, this high current is required to generate the required torque in the field weakening region.

B. Overload Consideration

The proposed design process with consideration of the OL capability is employed in this section. The optimal solutions of the optimization study over the three considered driving cycles are tabulated in Table V. The results demonstrate a smaller depth of the rotor and stator slots compared to the normal optimization results dimensions. The smaller back-iron and L_{st} are other factors which can be seen as the results of the consideration of the OL capability (see the axial views in Fig. 12).

The EffM of the designed machines over each investigated driving cycle are shown in Fig. 12. The rated current and maximum current to cover all the operating points of the considered driving cycles is highlighted in each presented EffM. It is seen that the maximum current of these designs is almost three times the rated value.

C. Comparison of the Designed IMs

Although the consideration of the OL operation for the designed electric machines for EVs is investigated in literature, a
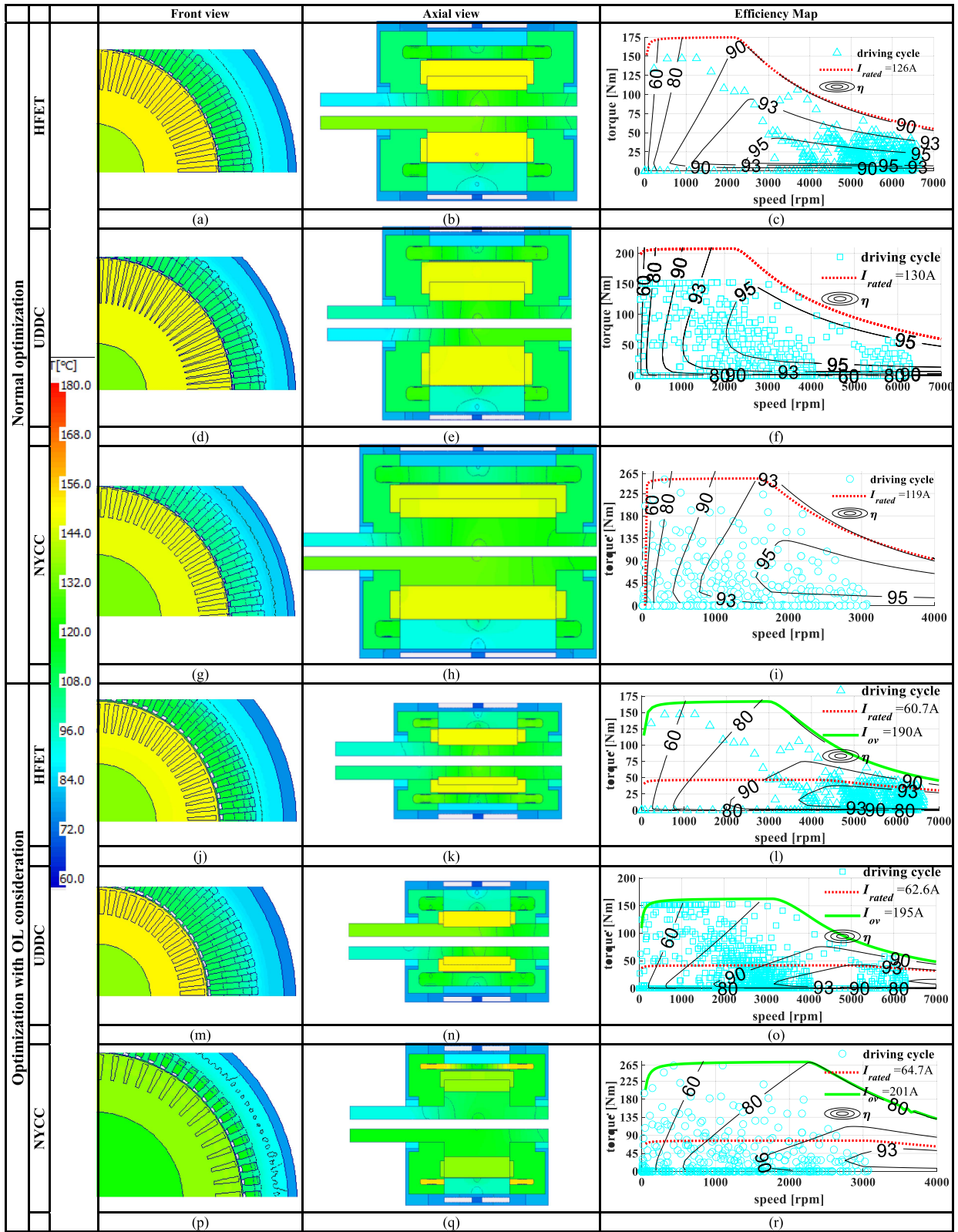
Fig. 12.   Comparison of the six optimised designs. Steady-state 3-D FEA results of thermal analysis at the rated current (1st and 2nd columns) and EffMs (3rd column). The axial view is shown to scale to indicate the comparative size of the six machines.
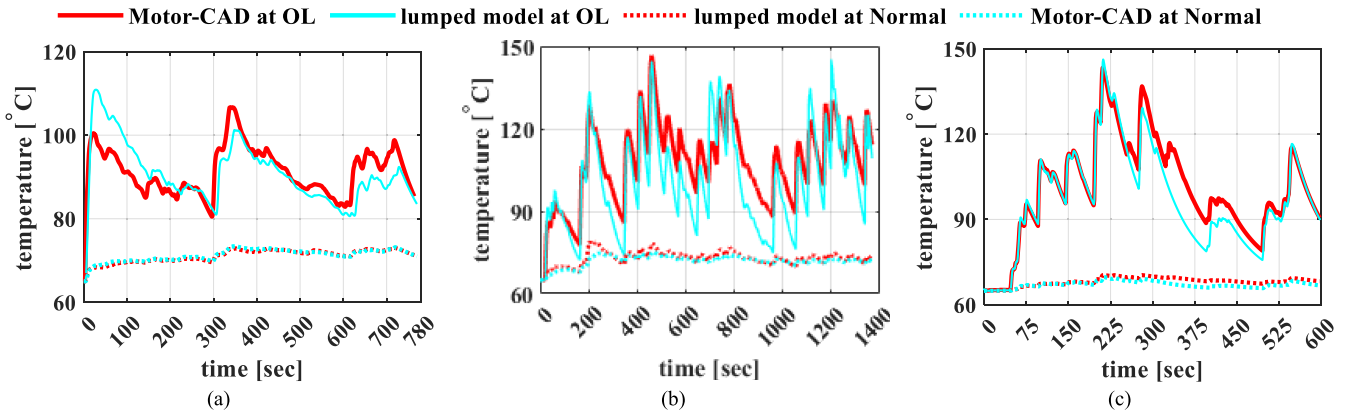
Fig. 13. Motor-CAD and lumped model results of the transient thermal analysis of the stator winding hotspot of the designed machines with and without consideration of OL (a) HFET, (b) UDDC, (c) NYCC.
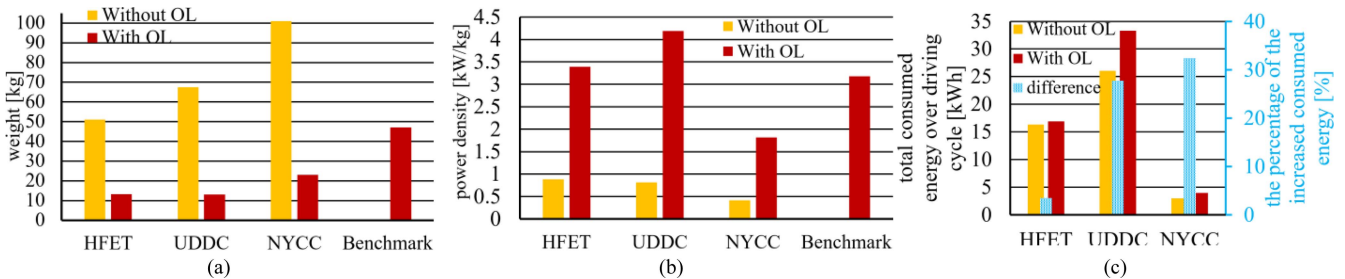

Fig. 14. Comparison of (a) weight of active materials (ignoring shaft weight) and (b) power density of the optimal designs with and without consideration of the overload during optimization against benchmark. (c) The total consumed energy in the six design and the energy consumption percentage by consideration of OL.

TABLE VI
THE MASS OF THE ACTIVE MATERIALS IN THE OPTIMAL DESIGNS

Part	HFET		UDDC		NYCC	
	Norm.	OL.	Norm.	OL.	Norm.	OL.
Stator steel [kg]	23.5	5.56	23.9	6.36	39.6	9.04
Stator copper [kg]	6.15	1.96	9.16	1.95	14.1	2.29
Rotor steel [kg]	12.6	3.61	22.8	2.79	29.9	8.72
Rotor copper[kg]	8.82	2.14	11.6	2.02	17.4	2.99
Shaft steel [kg]	7.64	5.02	8.38	4.63	17.3	9.56
Total weight [kg]	58.7	18.3	75.9	17.7	118	32.6

comparison between the differences with and without consideration of OL has not been explicitly reported. In this section, a comparison between the optimal designs with and without consideration of the OL condition is carried out to highlight their differences.

A transient thermal analysis during operation in the driving cycles is executed to check the reliability of the designs based on the suggested design process. The results of the transient thermal analysis are presented in Fig. 13. The class F insulation permits a hotspot temperature of 155°C for the winding. As shown in Fig. 10, all the designs operate within the temperature constraint of the Class F insulation. This figure shows the designed machines without consideration of OL have peak temperatures of less than about 80°C which is quite low. When larger torques are required in the driving cycle, the temperature of the machine

significantly increases because of the higher currents which flow through the rotor bars and windings.

The results of the proposed thermal model used during the optimization has been compared with the Motor-CAD transient thermal analysis results in Fig. 13. These results show the success of the thermal model in prediction of the temperature.

Table VI shows the weight of the active materials consisting of the iron parts and copper in both the stator and rotor in the optimal designs. The designs using the OL capability are much lighter than their counterparts. Fig. 14(a) compares the weight of the active materials including end-winding of the designed IMs using the normal optimization and OL consideration optimization. It demonstrates the weight of designed IMs for HFET, UDDC, and NYCC using normal optimization are respectively about 3.8, 5.1, and 4.4 times of the designed IMs with consideration of OL. This reduction of the weight leads to the increase of the power density which is reported in Fig. 14(b). The consideration of OL allows to reach about 4 to 5 times larger power density for the designed IMs for the HFET, UDDC, and NYCC driving cycles.

It should be noted that while using the overload capability of the machines can significantly reduce the machine size for a given driving cycle, there are likely other practical constraints like gradeability and continuous power requirements which may limit the ability to implement this fully in practice.
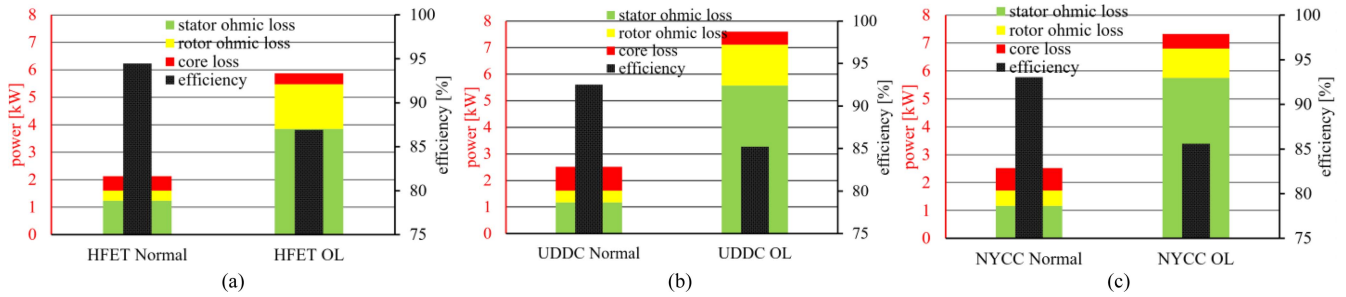
Fig. 15. Comparison of the loss breakdown and efficiency at the maximum power point operation of the optimal normal designs against OL designs for (a) HFET at 42.5kW, (b) UDDC at 47.2kW, and (c) NYCC at 46.4kW.

TABLE VII
EQUIVALENT CIRCUIT PARAMETERS OF THE OPTIMAL DESIGNS

EEC parameters	HFET		UDDC		NYCC	
	Norm.	OL.	Norm.	OL.	Norm.	OL.
R_s @ 140°C [Ω]	0.035	0.081	0.028	0.072	0.029	0.095
R_r' @ 140°C [Ω]	0.012	0.041	0.011	0.028	0.015	0.021
L_{ls} [mH]	0.111	0.144	0.114	0.175	0.172	0.105
L_{lr}' [mH]	0.202	0.231	0.209	0.194	0.271	0.263

Fig. 14(c) shows the efficiency drop when the IM designs based on OL are utilized in the EV instead of the normal optimal designs. It is seen that the energy consumption for the HFET is about four percent higher while for the UDDC and NYCC designs this is increased by 28% and 31%. This is because there are more operating points in the UDDC and NYCC which require larger torque than the rated power of the designs. As shown in the EffM of the OL-based design, the efficiency is substantially lower (e.g., 5-20%). Hence, in those driving cycles in which the EV requires large torque, the energy consumption increases significantly.

Table VII reports the electrical equivalent circuit parameters to show the difference and similarities of the designed IMs. It is seen that the leakage inductances of the IMs designed based on the normal optimization process and OL consideration procedure are close to each other for all three driving cycles. However, there is a large difference between the rotor and stator resistances with and without consideration of OL

The reported current values in the third column of Fig. 12 showed that the current increase can be a reason for the efficiency drop.

The higher resistance value of the OL considered designs against the normal designs is another reason for the efficiency reduction in the OL based designs (see Table VII). The maximum power in the torque-speed plane of each design is considered for the loss shown in Fig. 15. This figure shows at the considered operating point the amount of the loss in the OL considered designs is at least three times of the IMs designed without considered of OL.

D. Performance of the Designs in a Driving Cycle

This section describes the performance comparison for the designed motors for a specific vehicle driving cycle giving an
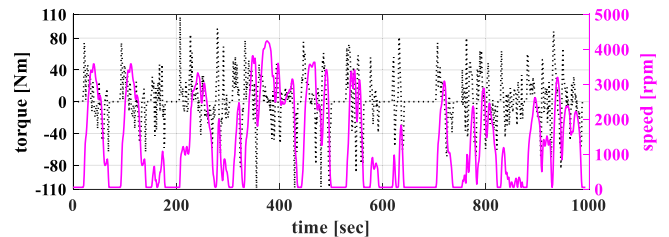

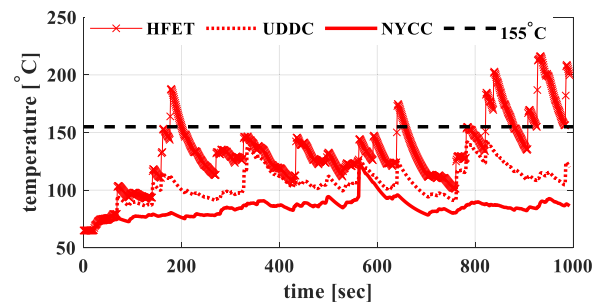Fig. 16. Artemis urban driving cycle operating points.

Fig. 17. The temperature variation during operation of the designed machines over operation in Artemis urban driving cycle.

indication on the range of torque requirements. It investigates the performance of the designed machines based on the OL consideration in the Artemis urban driving cycle [46]. For the considered gearbox system, the maximum motor speed for this driving cycle is 4,230 rpm and the maximum torque is 110 Nm (see Fig. 16). So, the designed machines can operate in this range from the electromagnetic perspective.

The temperature variation graph presented in Fig. 17 demonstrates the inability of HFET-based designed machine to operate over the Artemis urban driving cycle within the temperature limit. This is expected because this machine is designed based on HFET which is a highway-based driving cycle. Ignoring the thermal limit, not only the energy consumption of HFET-based design is largest compared to the other two driving cycles, but also it offers minimum efficiency (see Fig. 18).

The comparison of the energy consumption and efficiency of UDDC- and NYCC- based designs shows the lower energy consumption and higher efficiency of NYCC-based design. The maximum operating speed of the NYCC is close to the Artemis
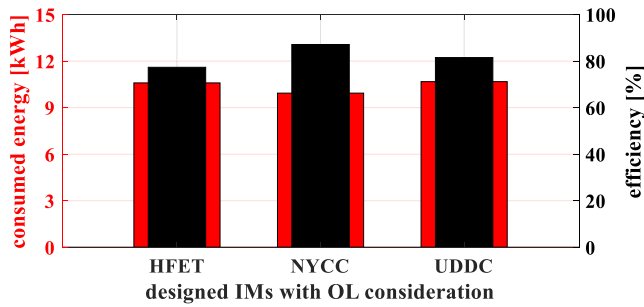
Fig. 18. The energy consumption and average efficiency of the OL-considered designs over the Artemis urban driving cycle.

urban driving cycle. This similarity leads to the better performance of this design.

E. Computation Time Comparison

The proposed optimization procedure utilizes a SDM model and a thermal model in each iteration. For a certain design, the required time for the SDM model to calculate the EffM is 23 seconds using a Core i9-7900X (3.30 GHz) computer with 128 GB RAM. The estimated driving cycle loss data are the inputs for thermal model. These data are extracted in 1 second from the output data of the SDM model. The thermal model predicts the temperature variation over a driving cycle in 28 seconds. Thus, the total required time for the proposed model to predict the electromagnetic and thermal behavior of a certain design is less than one minute.

On the same computer, FEA modeling in Motor-CAD requires 140, 180, 63, and 154 seconds for the saturation modelling, core loss modelling, efficiency map estimation, and driving cycle data extraction, respectively. The transient thermal analysis takes about 14 minutes to be completed in Motor-CAD. Thus, the total required time for analysis of an induction machine over driving cycle and estimation of its temperature variation is about 22 minutes for a certain design in Motor-CAD.

In the optimization procedure, around 3000 designs are analyzed for each driving cycle. Therefore, the total time of the simulation using the proposed analytical model is about 43 hours. On the other hand, Motor-CAD needs about 1100 hours for such an optimization study which is about 26 times of the proposed analytical model. Thus, the proposed analytical model is a computationally-efficient technique for the optimization of induction machines for traction applications.

VII. Conclusion

This paper discussed the optimization of induction motors over three specific vehicle driving cycles. An accurate multi-physics model was developed for performance parameter and temperature estimation of the IMs. The performance parameters were calculated using a subdomain model with capability of the prediction of saturation level at different operating points. The temperature variation was predicted using a lumped-circuit thermal model.

The main objective of the paper was to show the application of the proposed fast and accurate multi-physics model for the optimal design of IMs over a given driving cycle. Two sets of optimizations were executed. Firstly, the IMs were optimized for maximum efficiency in the minimum possible volume. Secondly, the IMs were optimized only for minimum volume while meeting the thermal limitations during the driving cycle. This resulted in increasing the power density by up to four times but also reduced the machine efficiency and increased the driving cycle energy consumption by about 30% for some cases. Note that the capability to use this approach to reduce the motor size will likely be limited by other vehicle constraints such as gradeability.

Although the OL performance is considered in the design of the electric motors in industrial applications, there is limited reported data on investigation of the OL effect in the literature. The presented results in this paper show that the energy consumption increases by consideration of OL in highway driving cycles (i.e., HFET) is only about 2.5% larger than the normal design. So, it is more reasonable to consider the minimum volume objective function for the EVs which are designed for highway applications. Although the results showed it is possible to achieve 4 times higher power density in the IMs designed for operation in urban area, the 30% increase in energy consumption is a limit to design for minimum volume. The energy consumption constraint can be added to the problem to cover this trade-off.

The experimental validation of the thermal model can be the subject of the study in future. Furthermore, the consideration of joint optimization to find the optimal designs with and without consideration of OL in parallel with each other can be the subject of future studies to speed up the design and comparison process.

References

[1] T. - V. Tran, E. Negre, K. Mikati, P. Pellerey, and B. Assaad, "Optimal design of TEFC induction machine and experimental prototype testing for city battery electric vehicle," *IEEE Trans. Ind. Appl.*, vol. 56, no. 1, pp. 635–643, Jan./Feb. 2020, doi: 10.1109/TIA.2019.2943447.

[2] K. Li, A. Bouscayrol, S. Cui, and Y. Cheng, "A hybrid modular cascade machines system for electric vehicles using induction machine and permanent magnet synchronous machine," *IEEE Trans. Veh. Technol.*, vol. 70, no. 1, pp. 273–281, Jan. 2021, doi: 10.1109/TVT.2020.3047219.

[3] R. Mistry, W. R. Finley, and T. Gaerke, "Comparison of IEC and NEMA requirements to ensure proper specification and design of induction motors & generators for global use-part 2: Copyright material IEEE, paper no. PCIC-2017-04," in *Proc. IEEE Petroleum Chem. Ind. Tech. Conf.*, 2018, pp. 29–38.

[4] A. Cavagnino, S. Vaschetto, L. Ferraris, Z. Gmyrek, E. Agamloh, and G. Bramerdorfer, "Towards an IE4 efficiency class for induction motors with minimal manufacturer impact," in *Proc. IEEE Energy Convers. Congr. Expo.*, 2018, pp. 289–296.

[5] T. A. Lipo, "Introduction to AC machine design," *Introduction to AC Mach. Des.*, vol. 9, pp. 193–250, 2017, doi: 10.1002/9781119352181.

[6] A. G. Sarigiannidis, M. E. Beniakar, and A. G. Kladas, "Fast adaptive evolutionary PM traction motor optimization based on electric vehicle drive cycle," *IEEE Trans. Veh. Technol.*, vol. 66, no. 7, pp. 5762–5774, Jul. 2017, doi: 10.1109/TVT.2016.2631161.

[7] T. Wu et al., "Multiobjective optimization of a tubular coreless LPMSM based on adaptive multiobjective black hole algorithm," *IEEE Trans. Ind. Electron.*, vol. 67, no. 5, pp. 3901–3910, May 2019.

[8] R. C. P. Silva, T. Rahman, M. H. Mohammadi, and D. A. Lowther, "Multiple operating points based optimization: Application to fractional slot concentrated winding electric motors," *IEEE Trans. Ind. Electron.*, vol. 65, no. 2, pp. 1719–1727, Feb. 2018, doi: 10.1109/TIE.2017.2756586.

[9] D. M. Ionel and M. Popescu, "Finite-element surrogate model for electric machines with revolving field-application to IPM motors," *IEEE Trans. Ind. Appl.*, vol. 46, no. 6, pp. 2424–2433, Jun. 2010, doi: 10.1109/TIA.2010.2073671.

[10] Q. Wang, F. Zhao, and K. Yang, "Analysis and optimization of the axial electromagnetic force for an axial-flux permanent magnet vernier machine," *IEEE Trans. Magn.*, vol. 57, no. 2, pp. 7–11, Feb. 2021, doi: 10.1109/TMAG.2020.3005216.

[11] K. Diao, X. Sun, G. Bramerdorfer, Y. Cai, G. Lei, and L. Chen, "Design optimization of switched reluctance machines for performance and reliability enhancements: A review," *Renewable Sustain. Energy Rev.*, vol. 168, 2022, Art. no. 112785.

[12] Z. Hao, W. Zhou, T. Ji, X. Huang, and C. Zhang, "Multi-objective optimization of double primary tubular permanent magnet synchronous linear motor in wide temperature range environment based on Pareto front method," *IEEE Access*, vol. 8, pp. 207193–207203, 2020, doi: 10.1109/AC-CESS.2020.3026040.

[13] R. C. P. Silva, M. Li, T. Rahman, and D. A. Lowther, "Surrogate-based MOEA/D for electric motor design with scarce function evaluations," *IEEE Trans. Magn.*, vol. 53, no. 6, Jun. 2017, Art. no. 7400704.

[14] Y. Ma, J. Wang, L. Zhou, and K. Shuai, "Surrogate-assisted optimization of a five-phase SPM machine with quasi-trapezoidal PMs," *IEEE Trans. Ind. Electron.*, vol. 69, no. 1, pp. 202–212, Jan. 2021.

[15] J. C. Son, J. Y. Kim, J. W. Choi, D. K. Lim, and H. K. Yeo, "Performance enhancement of the IPMSM for HEV applications using grain-oriented electrical steel and design optimization," *IEEE Access*, vol. 10, pp. 46599–46607, 2022, doi: 10.1109/ACCESS.2022.3170896.

[16] G. Lei, G. Bramerdorfer, B. Ma, Y. Guo, and J. Zhu, "Robust design optimization of electrical machines: Multi-objective approach," *IEEE Trans. Energy Convers.*, vol. 36, no. 1, pp. 390–401, Jan. 2021, doi: 10.1109/TEC.2020.3003050.

[17] G. Watthewaduge, E. Sayed, M. Bakr, A. Emadi, and B. Bilgin, "An optimization study for a switched reluctance motor using magnetic equivalent circuit and space mapping techniques," in *Proc. IEEE Transp. Electrific. Conf. Expo*, 2020, pp. 1025–1030, doi: 10.1109/ITEC48692.2020.9161619.

[18] J. Hou, W. Geng, Q. Li, and Z. Zhang, "3-D Equivalent magnetic network modeling and FEA verification of a novel axial-flux hybrid-excitation in-wheel motor," *IEEE Trans. Magn.*, vol. 57, no. 7, Jul. 2021, Art. no. 8106912, doi: 10.1109/TMAG.2021.3081830.

[19] J. Gao, L. Dai, and W. Zhang, "Improved genetic optimization algorithm with subdomain model for multi-objective optimal design of SPMSM," *CES Trans. Electric. Mach. Syst.*, vol. 2, no. 1, pp. 160–165, 2020, doi: 10.23919/tems.2018.8326463.

[20] S. A. Mohd Shafri et al., "Design and optimization of electromagnetic torque for a surface-mounted PMSM by using subdomain model and GA in electric vehicle application," in *Proc. 24th Int. Conf. Elect. Machines Syst.*, 2021, pp. 11–16, doi: 10.23919/ICEMS52562.2021.9634680.

[21] W. Tong, S. Wang, S. Dai, S. Wu, and R. Tang, "A quasi-three-dimensional magnetic equivalent circuit model of a double-sided axial flux permanent magnet machine considering local saturation," *IEEE Trans. Energy Convers.*, vol. 33, no. 4, pp. 2163–2173, Apr. 2018, doi: 10.1109/TEC.2018.2853265.

[22] S. P. Emami, E. Roshandel, A. Mahmoudi, and S. Khaourzade, "IPM motor optimization for electric vehicles considering driving cycles," in *Proc. 31st Australas. Universities Power Eng. Conf.*, 2021, pp. 1–5.

[23] E. Roshandel, A. Mahmoudi, S. Kahourzade, and W. Soong, "Analytical model and performance prediction of induction motors using subdomain technique," in *Proc. IEEE Energy Convers. Congr. Expo.*, 2020, pp. 3815–3822, doi: 10.1109/ECCE44975.2020.9235826.

[24] E. Devillers, J. L. Besnerais, T. Lubin, M. Hecquet, and J. - P. Lecointe, "An improved 2-D subdomain model of squirrel-cage induction machine including winding and slotting harmonics at steady state," *IEEE Trans. Magn.*, vol. 54, no. 2, Feb. 2018, Art. no. 8100612.

[25] E. Roshandel, A. Mahmoudi, S. Kahourzade, and W. L. Soong, "Saturation consideration in modeling of the induction machine using subdomain technique to predict performance," *IEEE Trans. Ind. Appl.*, vol. 58, no. 1, pp. 261–272, Jan. 2022, doi: 10.1109/TIA.2021.3125915.

[26] E. Roshandel, A. Mahmoudi, and S. Kahourzade, "2D subdomain model of the ladder linear induction machine with considering saturation effect," in *Proc. IEEE Energy Convers. Congr. Expo.*, 2021, pp. 4127–4134, doi: 10.1109/ECCE47101.2021.9595612.

[27] S. Kahourzade, A. Mahmoudi, E. Roshandel, and Z. Cao, "Optimal design of axial-flux induction motors based on an improved analytical model," *Energy*, vol. 237, 2021, Art. no. 121552, doi: 10.1016/j.energy.2021.121552.

[28] R. L. J. Sprangers, J. J. H. Paulides, B. L. J. Gysen, and E. A. Lomonova, "Magnetic saturation in semi-analytical harmonic modeling for electric machine analysis," *IEEE Trans. Magn.*, vol. 52, no. 2, Feb. 2015, Art. no. 8100410.

[29] P. Liang, F. Chai, Y. Li, and Y. Pei, "Analytical prediction of magnetic field distribution in spoke-type permanent-magnet synchronous machines accounting for bridge saturation and magnet shape," *IEEE Trans. Ind. Electron.*, vol. 64, no. 5, pp. 3479–3488, May 2016.

[30] B. Dianati, S. Kahourzade, and A. Mahmoudi, "Optimization of axial-flux induction motors for the application of electric vehicles considering driving cycles," *IEEE Trans. Energy Convers.*, vol. 35, no. 3, pp. 1522–1533, Sep. 2020, doi: 10.1109/TEC.2020.2976625.

[31] E. Roshandel, A. Mahmoudi, S. Kahourzade, and W. L. Soong, "Efficiency maps of electrical machines: A tutorial review," *IEEE Trans. Ind. Appl.*, vol. 59, no. 2, pp. 1263–1272, Mar./Apr. 2023, doi: 10.1109/TIA.2022.3210077.

[32] N. Flaherty, "Radial flux motors," *E-Mobility Engineering*, 2022. [Online]. Available: https://www.emobility-engineering.com/radial-flux-motors/

[33] Ansys Motor-CAD, "Electric machine design software," 2021. [Online]. Available: https://www.ansys.com/products/electronics/ansys-motor-cad

[34] G. S. Liew, *Analysis and Design of Single-Sided, Slotted AMM Axial-Field Permanent Magnet Machines*. Adelaide SA, Australia: Univ. of Adelaide, 2009.

[35] X. Ding, M. Bhattacharya, and C. Mi, "Simplified thermal model of PM motors in hybrid vehicle applications taking into account eddy current loss in magnets," *J. Asian Electric. Veh.*, vol. 8, no. 1, pp. 1337–1343, 2010, doi: 10.4130/jaev.8.1337.

[36] S. K. Chowdhury and P. K. Baski, "A simple lumped parameter thermal model for electrical machine of TEFC design," in *Proc. Joint Int. Conf. Power Electron., Drives Energy Syst. 2010 Power India*, 2010, pp. 1–7, doi: 10.1109/PEDES.2010.5712385.

[37] D. A. Staton and A. Cavagnino, "Convection heat transfer and flow calculations suitable for electric machines thermal models," *IEEE Trans. Ind. Electron.*, vol. 55, no. 10, pp. 3509–3516, Oct. 2008, doi: 10.1109/TIE.2008.922604.

[38] W. Brown and Y. Liu, "Modeling and simulation of an electric vehicle with independent rear motors to estimate the fuel economy during EPA drive cycles," *Int. J. Veh. Struct. Syst.*, vol. 12, no. 5, pp. 46–52, 2020.

[39] G. Bramerdorfer, J. A. Tapia, J. J. Pyrhonen, and A. Cavagnino, "Modern electrical machine design optimization: Techniques, trends, and best practices," *IEEE Trans. Ind. Electron.*, vol. 65, no. 10, pp. 7672–7684, Oct. 2018, doi: 10.1109/TIE.2018.2801805.

[40] S. G. Min, G. Bramerdorfer, and B. Sarlioglu, "Analytical modeling and optimization for electromagnetic performances of fractional-slot PM brushless machines," *IEEE Trans. Ind. Electron.*, vol. 65, no. 5, pp. 4017–4027, May 2018, doi: 10.1109/TIE.2017.2762627.

[41] M. G. Bijan and P. Pillay, "Efficiency estimation of the induction machine by particle swarm optimization using rapid test data with range constraints," *IEEE Trans. Ind. Electron.*, vol. 66, no. 8, pp. 5883–5894, Aug. 2019, doi: 10.1109/TIE.2018.2873121.

[42] F. Wang et al., "Design of model predictive control weighting factors for PMSM using Gaussian distribution-based particle swarm optimization," *IEEE Trans. Ind. Electron.*, vol. 69, no. 11, pp. 10935–10946, Nov. 2022, doi: 10.1109/TIE.2021.3120441.

[43] M. A. Jarrahi, E. Roshandel, M. Allahbakhshi, and M. Ahmadi, "Cost-optimal as a tool for helping in designing distribution transformer using particle swarm optimization," *Int. J. Comput. Math. Elect.. Electron. Eng.*, vol. 38, no. 2, pp. 862–877, Mar. 2019, doi: 10.1108/COM-PEL-06-2017-0229.

[44] Y. - L. Chen, J. Cheng, C. Lin, X. Wu, Y. Ou, and Y. Xu, "Classification-based learning by particle swarm optimization for wall-following robot navigation," *Neurocomputing*, vol. 113, pp. 27–35, 2013.

[45] E. Roshandel, A. Mahmoudi, S. Kahourzade, A. Tahir, and N. Fernando, "Propulsion system of electric vehicles: Review," in *Proc. Australas. Universities Power Eng. Conf.*, 2021, pp. 1–6.

[46] D. Maamria, K. Gillet, G. Colin, Y. Chamaillard, and C. Nouillant, "Optimal predictive eco-driving cycles for conventional, electric, and hybrid electric cars," *IEEE Trans. Veh. Technol.*, vol. 68, no. 7, pp. 6320–6330, Jul. 2019, doi: 10.1109/TVT.2019.2914256.